The WiggleZ Dark Energy Survey: the growth rate of cosmic structure since redshift $z = 0.9$

Chris Blake,[1]★ Sarah Brough,[2] Matthew Colless,[2] Carlos Contreras,[1] Warrick Couch,[1] Scott Croom,[3] Tamara Davis,[4,5] Michael J. Drinkwater,[4] Karl Forster,[6] David Gilbank,[7] Mike Gladders,[8] Karl Glazebrook,[1] Ben Jelliffe,[3] Russell J. Jurek,[9] I-hui Li,[1] Barry Madore,[10] D. Christopher Martin,[6] Kevin Pimbblet,[11] Gregory B. Poole,[1] Michael Pracy,[1,12] Rob Sharp,[2,12] Emily Wisnioski,[1] David Woods,[13] Ted K. Wyder[6] and H. K. C. Yee[14]

[1]*Centre for Astrophysics & Supercomputing, Swinburne University of Technology, PO Box 218, Hawthorn, VIC 3122, Australia*
[2]*Australian Astronomical Observatory, PO Box 296, Epping, NSW 1710, Australia*
[3]*Sydney Institute for Astronomy, School of Physics, University of Sydney, NSW 2006, Australia*
[4]*School of Mathematics and Physics, University of Queensland, Brisbane, QLD 4072, Australia*
[5]*Dark Cosmology Centre, Niels Bohr Institute, University of Copenhagen, Juliane Maries Vej 30, DK-2100 Copenhagen Ø, Denmark*
[6]*California Institute of Technology, MC 278-17, 1200 East California Boulevard, Pasadena, CA 91125, USA*
[7]*Astrophysics and Gravitation Group, Department of Physics and Astronomy, University of Waterloo, Waterloo, ON N2L 3G1, Canada*
[8]*Department of Astronomy and Astrophysics, University of Chicago, 5640 South Ellis Avenue, Chicago, IL 60637, USA*
[9]*Australia Telescope National Facility, CSIRO, Epping, NSW 1710, Australia*
[10]*Observatories of the Carnegie Institute of Washington, 813 Santa Barbara Street, Pasadena, CA 91101, USA*
[11]*School of Physics, Monash University, Clayton, VIC 3800, Australia*
[12]*Research School of Astronomy & Astrophysics, Australian National University, Weston Creek, ACT 2600, Australia*
[13]*Department of Physics & Astronomy, University of British Columbia, 6224 Agricultural Road, Vancouver, BC V6T 1Z1, Canada*
[14]*Department of Astronomy and Astrophysics, University of Toronto, 50 St George Street, Toronto, ON M5S 3H4, Canada*

ABSTRACT

We present precise measurements of the growth rate of cosmic structure for the redshift range $0.1 < z < 0.9$, using redshift-space distortions in the galaxy power spectrum of the WiggleZ Dark Energy Survey. Our results, which have a precision of around 10 per cent in four independent redshift bins, are well fitted by a flat Λ cold dark matter (ΛCDM) cosmological model with matter density parameter $\Omega_m = 0.27$. Our analysis hence indicates that this model provides a self-consistent description of the growth of cosmic structure through large-scale perturbations and the homogeneous cosmic expansion mapped by supernovae and baryon acoustic oscillations. We achieve robust results by systematically comparing our data with several different models of the quasi-linear growth of structure including empirical models, fitting formulae calibrated to N-body simulations, and perturbation theory techniques. We extract the first measurements of the power spectrum of the velocity divergence field, $P_{\theta\theta}(k)$, as a function of redshift (under the assumption that $P_{g\theta}(k) = -\sqrt{P_{gg}(k)P_{\theta\theta}(k)}$, where g is the galaxy overdensity field), and demonstrate that the WiggleZ galaxy–mass cross-correlation is consistent with a deterministic (rather than stochastic) scale-independent bias model for WiggleZ galaxies for scales $k < 0.3\,h\,\mathrm{Mpc}^{-1}$. Measurements of the cosmic growth rate from the WiggleZ Survey and other current and future observations offer a powerful test of the physical nature of dark energy that is complementary to distance–redshift measures such as supernovae and baryon acoustic oscillations.

Key words: surveys – cosmological parameters – large-scale structure of Universe.

1 INTRODUCTION

Recent cosmological observations have revealed significant gaps in our understanding of the physics of the Universe. A set of

★E-mail: cblake@astro.swin.edu.au

measurements including the anisotropies of the cosmic microwave background (CMB) radiation, the shape of the clustering power spectrum of galaxies, the brightness of distant supernovae and the projected scales of baryon acoustic oscillations have indicated the presence of a 'dark energy' component which is propelling the cosmic expansion into a phase of acceleration (for recent results see Komatsu et al. 2009; Guy et al. 2010; Reid et al. 2010; Percival et al. 2010).

The physical nature of dark energy is not yet understood. Several explanations have been put forward including the presence of smoothly distributed energy such as a cosmological constant or a quintessence scalar field, a large-scale modification to Einstein's theory of general relativity, or the effects of spatially varying curvature in an inhomogeneous Universe. Further observational data are required to distinguish clearly between the subtly varying predictions of these very different physical models (e.g. Linder 2005; Wang 2008; Wiltshire 2009).

One of the most important observational data sets for addressing this issue is the large-scale structure of the galaxy distribution. The clustering within this distribution arises through a process of gravitational instability which acts to amplify primordial matter fluctuations. The growth rate of this structure with time is a key discriminant between cosmological models (e.g. Linder & Jenkins 2003; Linder & Cahn 2007; Nesseris & Perivolaropoulos 2008). Two different physical dark energy scenarios with the same background cosmic expansion generally produce different growth rates of perturbations; hence, growth measurements are able to discriminate between models that are degenerate under geometric tests (Davis et al. 2007; Rubin et al. 2009).

The growth of cosmic structure is driven by the motion of matter, for which galaxies act as 'tracer particles'. These flows imprint a clear observational signature in galaxy surveys, known as redshift-space distortions, because the galaxy redshift is generated by not only the background cosmic expansion but also the peculiar velocity tracing the bulk flow of matter (Kaiser 1987; Hamilton 1998). As a consequence the two-point statistics of the galaxy distribution are anisotropic on large scales, where the amplitude of the anisotropy is related to the velocity of the bulk flow and hence to the growth rate of structure.

Many previous galaxy surveys have measured this anisotropy employing either the galaxy correlation function or power spectrum. In the relatively local Universe, exquisite studies at redshift $z \approx 0.1$ have been undertaken using data from the Two-degree Field Galaxy Redshift Survey (2dFGRS; Peacock et al. 2001; Hawkins et al. 2003; Percival et al. 2004) and the Sloan Digital Sky Survey (SDSS; Tegmark et al. 2004). The SDSS luminous red galaxy (LRG) sample enabled these measurements to be extended to somewhat higher redshifts $z \approx 0.35$ (Tegmark et al. 2006; Okumura et al. 2008; Cabre & Gaztanaga 2009). Noisier results have been achieved at greater look-back times up to $z \approx 1$ by surveys mapping significantly smaller cosmic volumes such as the 2dF-SDSS LRG and Quasar survey (2SLAQ; da Angela et al. 2008) and the VIMOS-VLT Deep Survey (VVDS; Guzzo et al. 2008).

The current observational challenge is to map the intermediate-redshift $0.3 < z < 1$ Universe with surveys of comparable statistical power to 2dFGRS and SDSS, so that accurate growth-rate measurements can be extracted across the full (hypothesized) redshift range for which dark energy dominates the cosmic dynamics. In order to achieve this goal we have constructed the WiggleZ Dark Energy Survey (Drinkwater et al. 2010), a new large-scale spectroscopic galaxy redshift survey, using the multi-object AAOmega fibre spectrograph at the 3.9-m Australian Astronomical Telescope.

The survey, which began in 2006 August, targets ultraviolet-selected (UV-selected) star-forming emission-line galaxies in several different regions around the sky and at redshifts $z < 1$. By covering a total solid angle of $1000\,\mathrm{deg}^2$ the WiggleZ Survey maps two orders of magnitude more cosmic volume in the $z > 0.5$ Universe than previous galaxy redshift surveys. This paper presents the current measurements of the growth rate of structure using the galaxy power spectrum of the survey. The data set will also permit many other tests of the cosmological model via baryon acoustic oscillations, the Alcock–Pacyznski effect, higher order clustering statistics and topological descriptors of the density field.

The improving statistical accuracy with which redshift-space distortions may be measured by observational data sets requires that the theoretical modelling of the data also advances. Recent reviews of this topic have been provided by Percival & White (2009) and Song & Percival (2009). In the linear clustering regime, in the large-scale limit, the theory is well understood (Kaiser 1987; Hamilton 1998). However, both simulations and observations have demonstrated that linear theory is a poor approximation across a wide range of quasi-linear scales encoding a great deal of clustering information (e.g. Jennings, Baugh & Pascoli 2011; Okumura & Jing 2011). The blind application of linear-theory modelling to current surveys would therefore result in a significant systematic error in the extraction of the growth rate and a potential misdiagnosis of the physical nature of dark energy.

Various methodologies have been employed for extending the modelling of redshift-space distortions to quasi-linear and non-linear scales. The classical approach – the so-called 'streaming model' (e.g. Hatton & Cole 1998) – modulates the linear-theory clustering with an empirical damping function characterized by a variable parameter, which is marginalized over when extracting the growth rate. This model has provided an acceptable statistical fit to many previous data sets, but the lack of a strong physical motivation for the empirical function could lead to systematic errors when the model is confronted by high-precision data.

In this paper we consider two alternatives. First, quasi-linear redshift-space distortions can be modelled by various physically motivated perturbation theory schemes (for recent reviews see Carlson, White & Padmanabhan 2009; Nishimichi et al. 2009). Given that the accuracy of some current perturbation techniques breaks down at a particular quasi-linear scale, leading to potentially large discrepancies at smaller scales, the range of validity of these models must be carefully considered. The second approach is to use numerical N-body simulations to produce fitting formulae for the density and velocity power spectra (Smith et al. 2003; Jennings et al. 2011), which enables models to be established across a wider range of scales. The main concern of this approach is that these fitting formulae may only be valid for the subset of cosmologies and galaxy formation models in which they were derived (an important point given the unknown nature of dark energy).

A further significant issue in the modelling of redshift-space distortions in the galaxy distribution is the 'galaxy bias' relation by which galaxies trace the matter overdensities that drive the velocities (e.g. Cole & Kaiser 1989). The typical assumption of a local, linear, deterministic bias, for which there is a good physical motivation on large scales (Scherrer & Weinberg 1998), may break down in the case of precise measurements of the clustering pattern on quasi-linear scales (Swanson et al. 2008), also potentially leading to systematic errors in growth-rate fits. In this study we consider the introduction of stochasticity to the bias relation by varying the galaxy–mass cross-correlation (Dekel & Lahav 1999). We note that further studies of the WiggleZ data set involving the bispectrum,

three-point correlation function, galaxy halo occupation distribution and comparison with numerical simulations will yield further constraints on the form of galaxy bias.

The aim of this paper is to use the existing range of redshift-space distortion models and galaxy power spectra from the WiggleZ Survey to derive measurements of the growth rate across the redshift range $z < 1$ that are robust against modelling systematics. We assume throughout a cosmological model consistent with the analysis of the latest measurements of the CMB by the *Wilkinson Microwave Anisotropy Probe* (Komatsu et al. 2009): a flat Universe described by general relativity with matter density $\Omega_m = 0.27$, cosmological constant $\Omega_\Lambda = 0.73$, baryon fraction $\Omega_b/\Omega_m = 0.166$, Hubble parameter $h = 0.72$, primordial scalar index of fluctuations $n_s = 0.96$ and total fluctuation amplitude $\sigma_8 = 0.8$. In addition to providing a good description of the temperature and polarization fluctuations in the CMB, this model yields a good fit to distance measurements from supernovae and baryon acoustic oscillations (Guy et al. 2010; Percival et al. 2010). In this paper we test if the same model also predicts the observed growth rate of structure. Future studies will explore simultaneous fits to these data sets using different dark energy models.

The layout of this paper is as follows. In Section 2 we present the measurements of the various observational statistics quantifying the anisotropic power spectrum. Section 3 summarizes the current theory of redshift-space distortions in Fourier space and introduces in more detail the models we will fit to the data. In Section 4 we carry out the parameter fitting focussing on the growth rate and the galaxy–mass cross-correlation. Section 5 presents an analysis of the moments of the power spectrum and extraction of the power spectrum of the velocity divergence field, and Section 6 lists our conclusions.

2 MEASUREMENTS

2.1 Sample

The WiggleZ Dark Energy Survey at the Australian Astronomical Telescope (Drinkwater et al. 2010) is a large-scale galaxy redshift survey of bright emission-line galaxies mapping a cosmic volume of the order of 1 Gpc^3 over redshift $z < 1$. The survey, which began in 2006 August and is scheduled to finish in 2011 January, will obtain of the order of 200 000 redshifts for UV-selected galaxies covering of the order of 1000 deg^2 of equatorial sky, using the AAOmega spectrograph (Sharp et al. 2006). The survey design is driven by the scientific goal of measuring baryon acoustic oscillations in the galaxy power spectrum at a significantly higher redshift than existing surveys. The target galaxy population is selected from UV imaging by the *Galaxy Evolution Explorer* (*GALEX*) satellite, matched with optical data from the SDSS and Red Cluster Sequence survey (RCS2; Gilbank et al. 2011) to provide an accurate position for fibre spectroscopy. Full details about the survey design, execution and modelling are provided by Blake et al. (2009), Drinkwater et al. (2010) and Blake et al. (2010).

In this paper we analyse a subset of the WiggleZ sample assembled up to the end of the 10A semester (2010 May). We include data from six survey regions – the 9-, 11-, 15-, 22-, 1- and 3-h regions – in the redshift range $0.1 < z < 0.9$, which together constitute a total sample of $N = 152\,117$ galaxies. Fig. 1 displays the distribution in right ascension and declination of the analysed sample for the six survey regions, where the grey-scale level corresponds to the relative redshift completeness. We divided the sample into four redshift slices of width $\Delta z = 0.2$ in order to map the evolution of the growth rate with redshift. The effective redshifts at which the clustering pattern was measured in each of these slices (evaluated
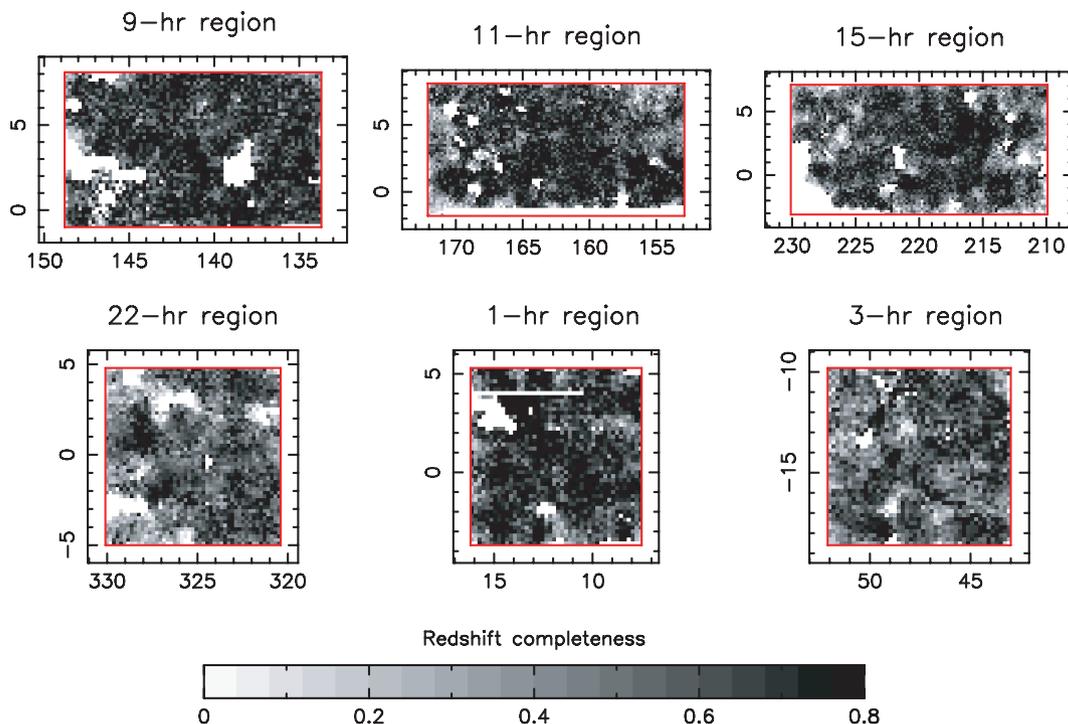
Figure 1. Grey-scale map illustrating the relative redshift completeness of each of the six WiggleZ Survey regions analysed in this paper. This figure is generated by taking the ratio of the galaxy densities in the redshift and parent catalogues in small cells. The *x*- and *y*-axes of each panel represent right ascension and declination, respectively.

using equation 44 of Blake et al. 2010) were $z_{\text{eff}} = (0.22, 0.41, 0.60, 0.78)$. The numbers of galaxies analysed in each redshift slice were $N = (19608, 39495, 60227, 32787)$.

2.2 Power-spectrum estimation

We estimated the two-dimensional galaxy power spectrum $P_g(k, \mu)$ in four redshift slices for each of the six WiggleZ Survey regions using the direct Fourier methods introduced by Feldman, Kaiser & Peacock (1994, hereafter FKP). Our methodology is fully described in section 3.1 of Blake et al. (2010); we give a brief summary here. First, we mapped the angle-redshift survey cone into a cuboid of comoving coordinates using a fiducial flat Λ cold dark matter (ΛCDM) cosmological model with matter density $\Omega_m = 0.27$. We gridded the catalogue in cells using nearest grid point assignment ensuring that the Nyquist frequencies in each direction were much higher than the Fourier wavenumbers of interest (we corrected the power-spectrum measurement for the small bias introduced by this gridding using the method of Jing 2005). We then applied a fast Fourier transform to the grid. The window function of each region was determined using the methods described by Blake et al. (2010) that model effects due to the survey boundaries, incompleteness in the parent UV and optical catalogues, incompleteness in the spectroscopic follow-up, systematic variations in the spectroscopic redshift completeness across the AAOmega spectrograph and variations of the galaxy redshift distribution with angular position. The fast Fourier transform of the window function was then used to construct the final power-spectrum estimator. The measurement was corrected for the small effect of redshift blunders using Monte Carlo survey simulations as described in section 3.2 of Blake et al. (2010).

Since each WiggleZ Survey region subtends a relatively small angle on the sky, of the order of $10°$, the flat-sky approximation is valid. We orient the x-axis of our Fourier cuboid parallel to the line of sight at the angular centre of each region, and then represent each Fourier mode by wavevectors parallel and perpendicular to the line of sight: $k_\parallel = |k_x|$ and $k_\perp = \sqrt{k_y^2 + k_z^2}$. We can also then determine the values of the total wavenumber of each mode $k = \sqrt{k_\parallel^2 + k_\perp^2}$ and the cosine of its angle to the line of sight, $\mu = k_\parallel/k$. We used two binning schemes for averaging the Fourier modes $\boldsymbol{k}$: in bins of $k_\perp$ and $k_\parallel$ (of width $0.02\,h\,\text{Mpc}^{-1}$) and in bins of k and μ (of width $0.02\,h\,\text{Mpc}^{-1}$ and 0.1, respectively). We determined the covariance matrix of the power-spectrum measurement in these binning schemes by implementing the sums in Fourier space described by FKP (see Blake et al. 2010, equations 20–22). The angular size of each WiggleZ region implies that the effect of wide-angle distortions (Raccanelli, Samushia & Percival 2010) is not significant.

We note that the FKP covariance matrix of the power spectrum only includes the contribution from the survey window function and neglects any covariance due to non-linear growth of structure or redshift-space effects. The full covariance matrix may be studied with the aid of a large ensemble of N-body simulations (Rimes & Hamilton 2005; Takahashi et al. 2011), which we are preparing in conjunction with the final WiggleZ Survey sample. The impact of using the full non-linear covariance matrix on growth-of-structure measurements has not yet been studied, although Takahashi et al. (2011) demonstrated that the effect on the accuracy of extraction of the baryon acoustic oscillations is very small.

The power-spectrum model must be convolved with the window function to be compared to the data. For reasons of computing speed, we recast the convolution as a matrix multiplication:

$$P_{\text{convolved}}(i) = \sum_j \mathbf{M}_{ij}\, P_{\text{model}}(j), \tag{1}$$

where i and j label a single bin in the two-dimensional set $(k_\perp, k_\parallel)$ or (k, μ). We determined the convolution matrix $\mathbf{M}_{ij}$ by evaluating the full Fourier convolution for a complete set of unit vectors. For example, to evaluate the jth row of matrix elements, corresponding to a bin $(k_{\text{min},j} < k < k_{\text{max},j}, \mu_{\text{min},j} < \mu < \mu_{\text{max},j})$, we defined the three-dimensional model in Fourier space for the unit vector

$$P_{\text{model}}(\boldsymbol{k}) = 1 \quad (k_{\text{min},j} < k < k_{\text{max},j}; \mu_{\text{min},j} < \mu < \mu_{\text{max},j}),$$
$$= 0 \quad \text{otherwise}, \tag{2}$$

applied the full convolution transform (equation 16 in Blake et al. 2010) and binned the resulting power-spectrum amplitudes in the same (k, μ) bins. The vector of results defines the jth row of the matrix $\mathbf{M}$ in equation (1). In summary, for each of the 24 subregions we obtain a data vector P_g^s [spanning $(k_\perp, k_\parallel)$ or (k, μ)], a covariance matrix and a convolution matrix.

Figs 2 and 3, respectively, display two-dimensional power spectra $P(k_\perp, k_\parallel)$ and $P(k, \mu)$ for each of the four redshift slices, obtained by stacking measurements across the six survey regions. For comparison we also plot in each case contours corresponding to the best-fitting non-linear empirical Lorentzian redshift-space distortion model described below. In Fig. 2 the non-circular nature of the measurements and models in Fourier space encode the imprint of redshift-space distortions. The overall 'squeezing' of the contours in the $k_\perp$ direction reflects the large-scale bulk flows. The apparent 'pinching' of the models near the $k_\parallel = 0$ axis is due to the damping caused by the pairwise velocity dispersion discussed below in Section 3.2, the amplitude of which is seen to increase with decreasing redshift (the pinching results from the relative variation with μ of the numerator and denominator of equation 10). Fig. 3, which bins the clustering amplitude with the cosine of the angle to the line of sight μ, illustrates how the coherent velocity flows boost the power of radial ($\mu = 1$) modes relative to tangential ($\mu = 0$) modes for a given scale k.

3 MODELLING THE REDSHIFT-SPACE GALAXY POWER SPECTRUM

In this section we describe a range of 18 models of the redshift-space galaxy power spectrum in the quasi-linear regime that we will try fitting to our measurements. These models are listed in Table 1. We assume that the shape of the underlying linear matter power spectrum is accurately determined by observations of the CMB radiation, and hence we fix the background cosmological parameters. In this case, each redshift-space power-spectrum model contains at least two parameters to be fitted: the growth rate f and a linear bias b. In several cases discussed below we introduce a third parameter, a variable damping coefficient σ_v. The multipole power spectra of these models at redshift $z = 0.6$ are compared in Fig. 4 assuming a linear bias $b = 1$, a growth rate $f = 0.7$ and (where applicable) a damping term $\sigma_v = 300\,h\,\text{km}\,\text{s}^{-1}$. For the purposes of illustration, all models in Fig. 4 are divided by a smooth 'no-wiggles' reference power spectrum from the fitting formulae of Eisenstein & Hu (1998), which has the same shape as the linear power spectrum but without the imprint of baryon acoustic oscillations.
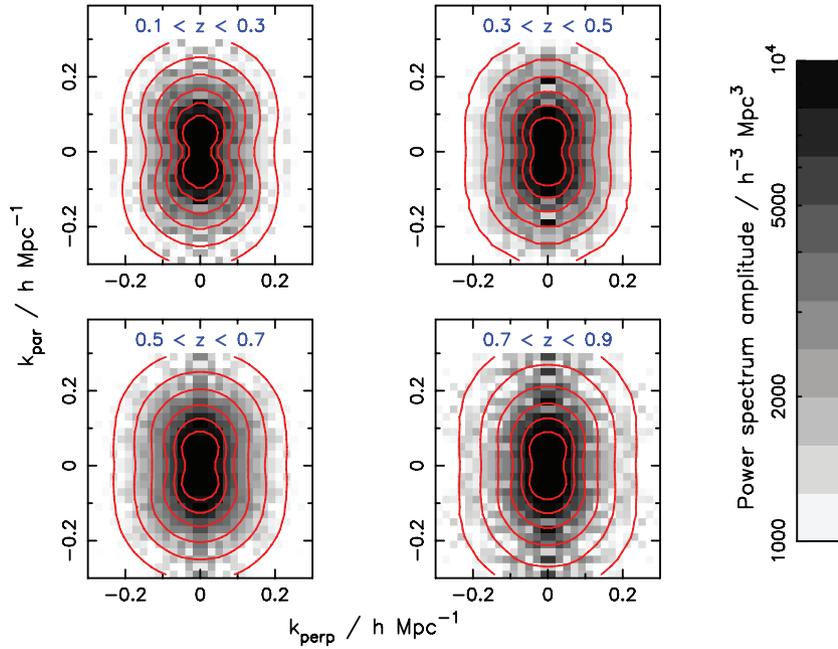
Figure 2. The galaxy power-spectrum amplitude as a function of wavevectors ($k_\perp$, $k_\parallel$) perpendicular and parallel to the line of sight, determined by stacking observations in different WiggleZ Survey regions in four redshift slices. The contours correspond to the best-fitting non-linear empirical Lorentzian redshift-space distortion model. We note that because of the differing degrees of convolution in each region due to the window function, a 'deconvolution' method was used to produce this plot. Before stacking, the data points were corrected by the ratio of the unconvolved and convolved two-dimensional power spectra corresponding to the best-fitting model for the purposes of this visualization. Only the top-right quadrant of data for each redshift is independent; the other three quadrants are mirrors of this first quadrant. The $k_\perp = 0$ axis is noisiest because it contains the lowest number of Fourier modes available for power-spectrum determination.
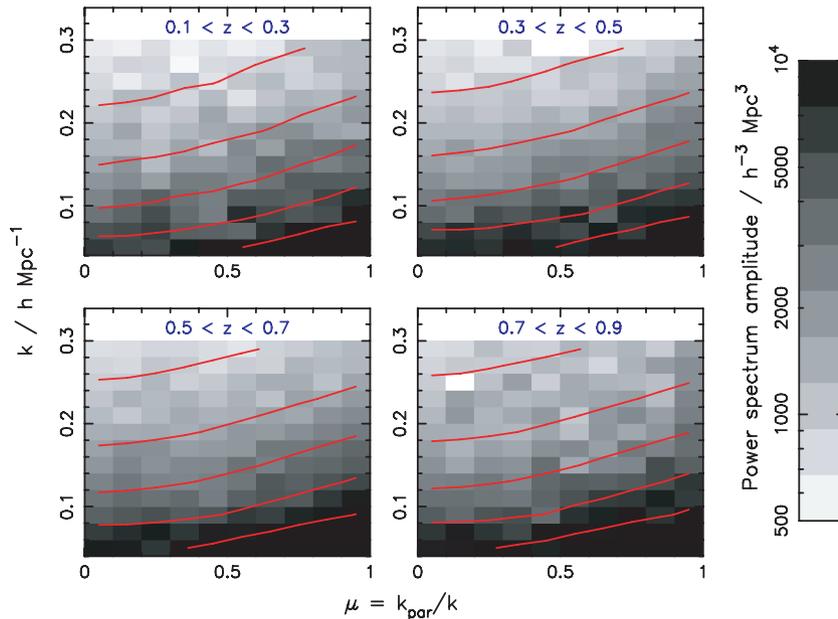
Figure 3. The galaxy power spectrum as a function of amplitude and angle of Fourier wavevector (k, μ), determined by stacking observations in different WiggleZ Survey regions in four redshift slices. The contours correspond to the best-fitting non-linear empirical Lorentzian redshift-space distortion model. A similar stacking method was used to that employed in the generation of Fig. 2. In the absence of redshift-space distortions, the model contours would be horizontal lines.

3.1 Density and velocity power spectra

The galaxy overdensity field, δ_g, is modified in redshift space by peculiar velocities. In Fourier space, the redshift-space overdensity field is given by

$$\delta_g^s(k, \mu) = \delta_g(k) - \mu^2\theta(k), \tag{3}$$

Table 1. Description of the quasi-linear redshift-space power-spectrum models fitted to the WiggleZ Survey measurements to determine the growth rate f. The 'damping' for each model can be 'variable' (empirically fitted to the data), 'linear' (determined using equation 12 as motivated by Scoccimarro 2004) or 'none' (not included in the model). In each model we also fit for a linear bias parameter b.

	Model	Damping	Fitted parameters	Reference
1	Empirical Lorentzian with linear $P_{\delta\delta}(k)$	Variable	f, b, σ_v	Hatton & Cole (1998)
2	Empirical Lorentzian with non-linear $P_{\delta\delta}(k)$	Variable	f, b, σ_v	
3	$P_{\delta\delta}, P_{\delta\theta}, P_{\theta\theta}$ from one-loop SPT	None	f, b	Vishniac (1983), Juszkiewicz, Sonoda & Barrow (1984)
4	$P_{\delta\delta}, P_{\delta\theta}, P_{\theta\theta}$ from one-loop SPT	Variable	f, b, σ_v	
5	$P_{\delta\delta}, P_{\delta\theta}, P_{\theta\theta}$ from one-loop SPT	Linear	f, b	
6	$P_{\delta\delta}, P_{\delta\theta}, P_{\theta\theta}$ from one-loop RPT	None	f, b	Crocce & Scoccimarro (2006)
7	$P_{\delta\delta}, P_{\delta\theta}, P_{\theta\theta}$ from one-loop RPT	Linear	f, b	
8	$P_{\delta\delta}, P_{\delta\theta}, P_{\theta\theta}$ from two-loop RPT	None	f, b	
9	$P_{\delta\delta}, P_{\delta\theta}, P_{\theta\theta}$ from two-loop RPT	Variable	f, b	
10	$P_{\delta\delta}, P_{\delta\theta}, P_{\theta\theta}$ from two-loop RPT	Linear	f, b	
11	$P(k, \mu)$ from one-loop SPT	None	f, b	Matsubara (2008)
12	$P(k, \mu)$ from one-loop SPT	Linear	f, b	
13	$P(k, \mu)$ with additional corrections	None	f, b	Taruya, Nishimichi & Saito (2010)
14	$P(k, \mu)$ with additional corrections	Variable	f, b, σ_v	
15	$P(k, \mu)$ with additional corrections	Linear	f, b	
16	Fitting formulae from N-body simulations	None	f, b	Smith et al. (2003), Jennings et al. (2011)
17	Fitting formulae from N-body simulations	Variable	f, b, σ_v	
18	Fitting formulae from N-body simulations	Linear	f, b	
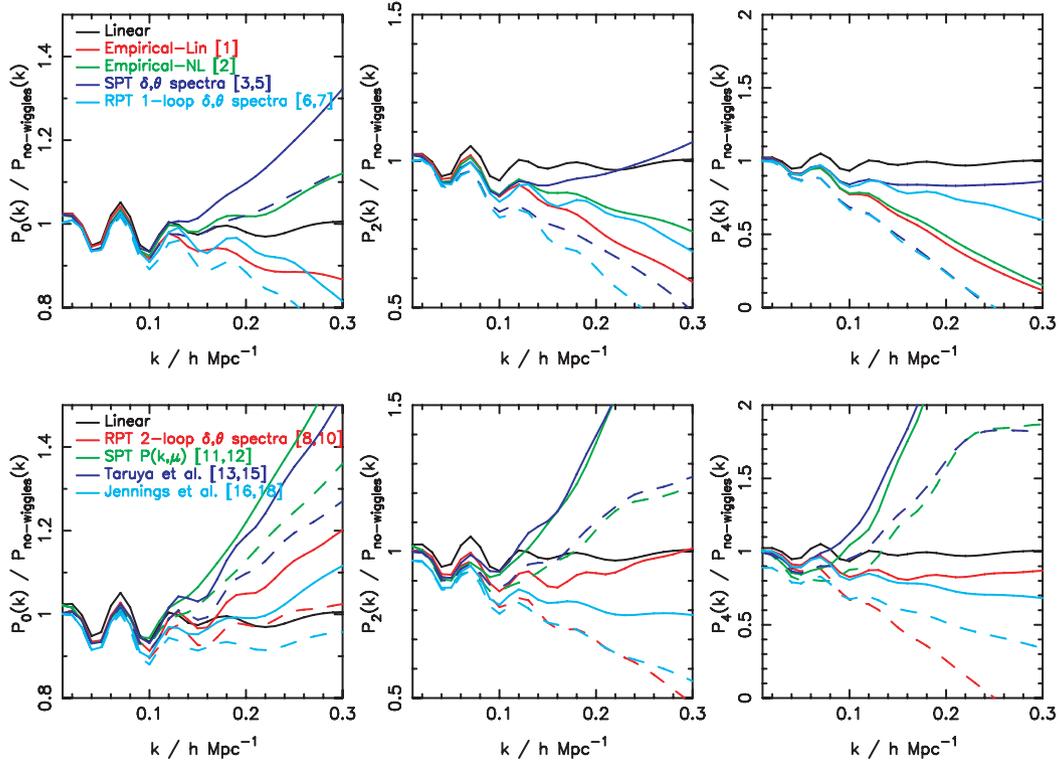
Figure 4. The multipole power spectra $P_\ell(k)$ for $\ell = 0, 2, 4$ for the different models listed in Table 1. The models are evaluated at redshift $z = 0.6$ assuming a linear bias $b = 1$, a growth rate $f = 0.7$ and (where applicable) a damping term $\sigma_v = 300\,h\,\mathrm{km\,s^{-1}}$. The models are labelled by their row number in Table 1. The solid and dashed lines are models that, respectively, include and exclude the damping term. All models are divided by a smooth 'no-wiggles' reference power spectrum from the fitting formulae of Eisenstein & Hu (1998), which has the same shape as the linear power spectrum but without the imprint of baryon acoustic oscillations. The models agree well in the large-scale limit, but significant differences develop between the models at smaller scales.

where $\theta(k)$ is the Fourier transform of the divergence of the peculiar velocity field $\boldsymbol{u}$ in units of the comoving Hubble velocity (i.e. $\boldsymbol{u} = \boldsymbol{v}/[H(a)a]$), $\theta = \nabla \cdot \boldsymbol{u}$, and μ is the cosine of the angle of the Fourier mode to the line of sight. Equation (3) assumes that the galaxy separation is small compared with the distance to the galaxies, δ_g and θ are small, the velocity field $\boldsymbol{u}$ is irrotational, and the continuity equation holds. In this case the linear redshift-space power spectrum of a population of galaxies may be written as

$$P_g^s(k, \mu) = P_{gg}(k) - 2\mu^2 P_{g\theta}(k) + \mu^4 P_{\theta\theta}(k), \tag{4}$$

where $P_{gg}(k) \equiv \langle |\delta_g(\boldsymbol{k})|^2 \rangle$, $P_{g\theta}(k) \equiv \langle \delta_g(\boldsymbol{k})\theta^*(\boldsymbol{k}) \rangle$ and $P_{\theta\theta}(k) \equiv \langle |\theta(\boldsymbol{k})|^2 \rangle$ are the isotropic galaxy–galaxy, galaxy–θ and θ–θ power

spectra for modes $\boldsymbol{k}$, respectively. We will often refer to the $P_{\theta\theta}(k)$ as the 'velocity power spectrum,' although it would be better described as the 'power spectrum of the velocity divergence field'.

Assuming that the velocity field is generated under linear perturbation theory then

$$\theta(k) = -f\,\delta(k), \tag{5}$$

where f is the growth rate of structure, expressible in terms of the growth factor $D(a)$ at the cosmic scale factor a as $f \equiv \mathrm{d}\ln D/\mathrm{d}\ln a$, and δ is the matter overdensity. The growth factor is defined in terms of the amplitude of a single perturbation as $\delta(a) = D(a)\,\delta(1)$. Equation (5) additionally assumes that the linearized Euler and Poisson equations hold in a perturbed Friedmann–Robertson–Walker universe. It represents a coherent flow of matter in which there is a one-to-one coupling between the Fourier components of the velocity divergence and density fields.

Under the assumption of a deterministic, scale-independent, local, linear bias b then

$$\delta_{\mathrm{g}} = b\,\delta, \tag{6}$$

and we may write $P_{gg} = b^2 P_{\delta\delta}$ and $P_{g\theta} = b\,P_{\delta\theta}$. If we additionally assume that equation (5) applies, then equation (4) may be written as

$$
\begin{aligned}
P_g^s(k,\mu) &= b^2\,P_{\delta\delta}(k)\left(1 + \frac{f\mu^2}{b}\right)^2 \\
&= b^2\,P_{\delta\delta}(k)\,(1 + \beta\mu^2)^2.
\end{aligned}
\tag{7}
$$

Equation (7) is known as the large-scale 'Kaiser limit' of the redshift-space power-spectrum model (Kaiser 1987), often expressed in terms of the parameter $\beta = f/b$. We assume no velocity bias between galaxies and matter (Lau, Nagai & Kravtsov 2010).

Simulations and observations have demonstrated that equation (7) is an unreliable model on all but the largest scales (smallest values of k) due to the non-linear growth of structure. Deviations from the Kaiser limit are evident for $k > 0.02\,h\,\mathrm{Mpc}^{-1}$ and are particularly noticeable in the θ power spectra (Jennings et al. 2011; Okumura & Jing 2011). This failure of the model is due to the breakdown of the relation between θ and δ (equation 5) rather than the underlying structure of equation (4) (Scoccimarro 2004). Non-linear evolution implies that a given overdensity δ produces a range of values of θ, and this range of velocities acts to smooth the galaxy overdensity field in redshift space, or damp the θ power spectra. This non-linear damping must be modelled in order to avoid introducing a systematic error into our extraction of the growth rate f from data. A variety of methods are available for implementing this non-linear correction, which we discuss below.

3.2 The empirical non-linear velocity model

The standard 'streaming model' for describing the non-linear component of redshift-space distortions (e.g. Hatton & Cole 1998) introduces an empirical damping function F to be multiplied into equation (4), representing convolution with uncorrelated galaxy motions on small scales:

$$P_g^s(k,\mu) = [P_{gg}(k) - 2\mu^2 P_{g\theta}(k) + \mu^4 P_{\theta\theta}(k)]F(k,\mu). \tag{8}$$

The two models most commonly considered in the literature are the Lorentzian $F = [1 + (k\sigma_v\mu)^2]^{-1}$ and the Gaussian $F = \exp[-(k\sigma_v\mu)^2]$, representing exponential and Gaussian convolutions in configuration space, and each parametrized by a single

variable σ_v. The Lorentzian model produces better fits to data (e.g. Hawkins et al. 2003; Cabre & Gaztanaga 2009) and we assume this version of the model in our study.

Equation (8) is typically applied assuming that P_{gg}, $P_{g\theta}$ and $P_{\theta\theta}$ are predicted by linear theory assuming equation (5); hence for the Lorentzian model we obtain

$$P_g^s(k,\mu) = b^2\,P_{\delta\delta,\mathrm{lin}}(k)\frac{(1 + f\mu^2/b)^2}{1 + (k\sigma_v\mu)^2}, \tag{9}$$

where we generated the linear power spectrum $P_{\delta\delta,\mathrm{lin}}(k)$ using the CAMB software package (Lewis, Challinor & Lasenby 2000). This is Model 1 in Table 1. We also considered the case where a nonlinear density power spectrum $P_{\delta\delta,\mathrm{NL}}(k)$, generated by applying the fitting formula of Smith et al. (2003) to the CAMB output, is used in equation (9):

$$P_g^s(k,\mu) = b^2\,P_{\delta\delta,\mathrm{NL}}(k)\frac{(1 + f\mu^2/b)^2}{1 + (k\sigma_v\mu)^2}\,. \tag{10}$$

This is Model 2.

Although these models are motivated by virialized motions of particles in collapsed structures, it is important to note that they are heuristic in nature. The correction represented by $F(k)$ in fits to real data is typically of the order of 20 per cent at $k \sim 0.2\,h\,\mathrm{Mpc}^{-1}$. These Fourier modes describe physical scales of tens of h^{-1} Mpc, far exceeding the size of virialized structures. In addition, the form of F and the value of σ_v depend strongly on details such as galaxy type, dark matter halo mass and satellite fraction. However, it should be noted that equation (9) does a very reasonable job of empirically modelling real data sets at the precision available in previous redshift surveys (e.g. Hawkins et al. 2003; Cabre & Gaztanaga 2009).

3.3 Perturbation theory approaches

A different approach to modelling clustering beyond linear scales is to extend equations (4) and (5) into the quasi-linear regime using perturbation theory techniques. These approaches have the advantage of a stronger physical motivation compared to the empirical streaming models, and the disadvantage that they are potentially applicable for a narrower range of scales, depending on the type of perturbation expansion. Standard perturbation theory (SPT) at $z = 0$ is only accurate for the range $k < 0.1\,h\,\mathrm{Mpc}^{-1}$, but other expansion approaches are available with the precise range of validity dependent on the model in question and the accuracy required (Carlson et al. 2009; Nishimichi et al. 2009). We describe the order of the perturbative expansion by the number of 'loops' of resummation performed; calculations including up to two loops are currently tractable.

Various methodologies have been introduced. The simplest technique is to use perturbation theory approaches to model the quasi-linear behaviour of the functions $P_{\delta\delta}(k)$, $P_{\delta\theta}(k)$ and $P_{\theta\theta}(k)$ in equation (4). These techniques have been recently reviewed by Nishimichi et al. (2009) and Carlson et al. (2009) and include Eulerian SPT (e.g. Vishniac 1983; Juszkiewicz et al. 1984) together with attempts to improve the convergence behaviour such as renormalized perturbation theory (RPT; e.g. Crocce & Scoccimarro 2006) which does not expand on the amplitude of fluctuations. When generating the perturbation theory predictions we assumed an input linear power spectrum consistent with the latest CMB observations:

$\Omega_m = 0.27$, $\Omega_\Lambda = 0.73$, $\Omega_b/\Omega_m = 0.166$, $h = 0.72$, $n_s = 0.96$ and $\sigma_8 = 0.8$.[1]

Going beyond the linear assumption may also lead to an alternative dependence of the redshift-space power spectrum on μ to that exhibited by equation (4). Scoccimarro (2004) proposed the following model for the redshift-space power spectrum in terms of the quasi-linear density and velocity power spectra:

$$P_g^s(k, \mu) = [P_{gg}(k) - 2\mu^2 P_{g\theta}(k) + \mu^4 P_{\theta\theta}(k)]e^{-(k\mu\sigma_v)^2} , \qquad (11)$$

where σ_v is determined by

$$\sigma_v^2 = \frac{1}{6\pi^2} \int P_{\theta\theta}(k) \, dk . \qquad (12)$$

The power spectra $P_{gg}(k)$, $P_{g\theta}(k)$ and $P_{\theta\theta}(k)$ in equation (11) may be generated by perturbation theory or other approaches. We note that $P_{g\theta}(k)$ and $P_{\theta\theta}(k)$ are functions of f. The damping factor in equation (11) is analogous to the streaming model of equation (8) but has a very different physical motivation: it aims to model the quasi-linear growth of the power spectra rather than virialized small-scale motions. Indeed, it would be possible to add an extra empirical damping factor F to equation (11) to model small-scale motions.

As discussed by Scoccimarro (2004), the model of equation (11) is an approximation in which the Gaussian damping factor attempts to reproduce the correct non-linear behaviour; equation (11) cannot be strictly derived from theory. Given this approximation we consider fitting σ_v as a variable parameter in addition to fixing it using equation (12). Models 3–10 in Table 1 are various combinations of SPT and RPT with different implementations of the damping term.

We note that σ_v can also be expressed in velocity units by multiplying by the Hubble parameter $H_0 = 100 \, h \, \text{km s}^{-1} \, \text{Mpc}^{-1}$. When calculating the damping term we use the linear velocity power spectrum as the input to equation (12), i.e. we set $P_{\theta\theta}(k) = f^2 P_{\delta\delta,\text{lin}}(k)$.

The final perturbation theory approaches we consider follow Matsubara (2008) and Taruya et al. (2010), who present quasi-linear perturbation theory models including terms up to μ^6, of the form

$$P_g^s(k, \mu) = \sum_{n=0}^{3} A_n(k) \mu^{2n}, \qquad (13)$$

where the coefficients $A_n(k)$ are the functions of f. The Matsubara (2008) results are a full angle-dependent treatment of SPT (Models 11 and 12), and Taruya et al. (2010) present an improved analysis incorporating additional correction terms (Models 13–15). When calculating the Taruya et al. model prediction we use power spectra $P_{\delta\delta}(k)$, $P_{\delta\theta}(k)$ and $P_{\theta\theta}(k)$ generated by two-loop RPT.

3.4 Fitting formulae calibrated by simulations

Finally, N-body dark matter simulations can be exploited to calibrate the quasi-linear forms of the functions $P_{\delta\delta}(k)$, $P_{\delta\theta}(k)$ and $P_{\theta\theta}(k)$. The advantage of this technique is that the results will be (potentially) reliable across a wider range of scales than is accessible with perturbation theory. The disadvantage is that simulations are expensive to generate and it is difficult to span a wide range of

input cosmological models (although that is not a limitation for us given that we are only considering a single fiducial model).

Smith et al. (2003) presented a widely used prescription for generating non-linear density power spectra $P_{\delta\delta}$. Fitting formulae calibrated to N-body simulations for $P_{\delta\theta}$ and $P_{\theta\theta}$ as a function of redshift, in terms of $P_{\delta\delta}$, were recently proposed by Jennings et al. (2011). We inserted these fitting functions into equation (11), scaling by f and f^2, respectively, to correct for the differing notation conventions. The Jennings et al. formulae, combined with various implementations of the damping term, are Models 16–18 in Table 1.

## 4 PARAMETER FITS

4.1 Growth rate

We fitted the 18 models introduced in Section 3 and summarized in Table 1 to the WiggleZ Survey galaxy power spectra $P_g(k_\perp, k_\parallel)$ measured in Section 2. For each of the four redshift slices we determined the growth rate f fitting to the six survey regions, marginalizing over the linear bias b (and the pairwise velocity dispersion σ_v where applicable). We also recorded the minimum value of the χ^2 statistic for each model calculated using the full covariance matrix. We repeated this procedure varying the range of scales $0 < \sqrt{k_\perp^2 + k_\parallel^2} < k_{\text{max}}$ over which each model is fitted. Utilizing a higher value of k_{max} produces an improved statistical error in the measurement, but potentially causes a larger systematic error since all models (and particularly some of the perturbation-theory models) are less reliable at larger values of k for which the non-linear corrections are more significant. In the absence of systematic errors, the best-fitting growth rate would be independent of k_{max}.

Fig. 5 displays the growth-rate measurements for the $0.5 < z < 0.7$ redshift slice (which produces the highest statistical accuracy of the four slices), comparing results for $k_{\text{max}} = 0.1$, 0.2 and $0.3 \, h \, \text{Mpc}^{-1}$. At least one model can always be found that provides a good fit to the data for each of the choices of k_{max}, as indicated by the minimum values of $\chi^2 = (93.8, 436.5, 999.1)$ for $k_{\text{max}} = (0.1, 0.2, 0.3)$ with the number of degrees of freedom (87, 411, 981). The respective probabilities for obtaining values of χ^2 higher than these are (0.29, 0.19, 0.34), indicating an acceptable goodness of fit. In Fig. 5 we display the minimum values of χ^2 for every model relative to the best-fitting model for each choice of k_{max}.

For $k_{\text{max}} = 0.1$ all models provide a good fit to the data and consistent measurements of the growth rate. This confirms the convergence of the different modelling approaches at large scales. For $k_{\text{max}} = 0.2$ and 0.3 some models are significantly disfavoured by larger values of χ^2, and these models produce measurements of the growth rate which systematically differ from the best performing models. For $k_{\text{max}} = 0.3$, models with a variable damping parameter produce a fit with a significantly lower value of χ^2, suggesting that equation (12) produces an unreliable prediction of the damping coefficient for these smaller scales.

Considering all four redshift slices, the best performing models for $k_{\text{max}} = 0.3 \, h \, \text{Mpc}^{-1}$ are the Taruya et al. (2010) model, incorporating extra angle-dependent correction terms in addition to the density and velocity power spectra from two-loop RPT (Model 14 in Table 1), and the Jennings et al. (2011) fitting formula calibrated from N-body simulations (Model 17). The growth rates deduced from these two very different modelling techniques agree remarkably well, after marginalizing over the variable damping term and linear galaxy bias, with the difference in values being much smaller

---
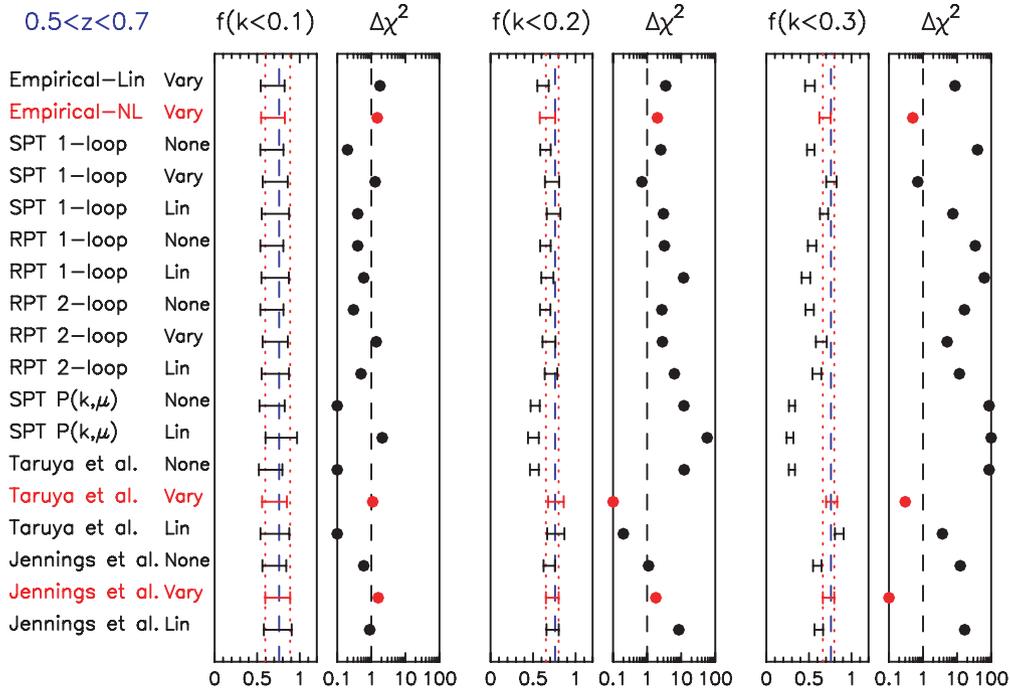
Figure 5. Measurements of the growth rate f for the $0.5 < z < 0.7$ redshift slice for each of the 18 models listed in Table 1. The three panels, each consisting of a pair of plots, correspond to different ranges of fitted scales $0 < k < k_{max}$, where $k_{max} = 0.1, 0.2$ and $0.3\,h\,\mathrm{Mpc}^{-1}$. For each panel, the left-hand plot shows the measurement of f and the right-hand plot displays the minimum value of the χ^2 statistic relative to the best-fitting model for that choice of k_{max}. In the left-hand plot, the vertical dashed line indicates the prediction of a flat ΛCDM cosmological model with $\Omega_m = 0.27$. The two vertical dotted lines span the 68 per cent confidence region of the growth rate measured for the Jennings et al. model with a variable damping parameter, facilitating an easy comparison of the results for different models. In the right-hand plot, points with $\Delta\chi^2 < 0.1$ are plotted at the left-hand edge of the panel and $\Delta\chi^2 = 1$ is indicated by the vertical dashed line. The three best performing models for $k_{max} = 0.3$ are highlighted by the red text.

than the statistical errors in the measurement. The level of this agreement gives us confidence that our results are not limited by systematic errors. We note that the empirical Lorentzian streaming model, where we use the non-linear model power spectrum, also performs well (Model 2 in Table 1). In Fig. 5 we have highlighted these three models in red. For all scales and redshifts, these models typically produce mutually consistent measurements of the growth rate and minimum values of χ^2 which differ by $\Delta\chi^2 \sim 1$. As a further comparison, Fig. 6 illustrates the measurements for all 18 models in every redshift slice for $k_{max} = 0.2$, again highlighting the same three optimal models in red.

We can use the dispersion in the results of fitting these three models to estimate the systematic error in the growth-rate measurement, by taking the variance of the different growth rates weighting by $\exp(-\chi^2/2)$. The systematic error in f calculated in this manner is $(0.01, 0.04, 0.03, 0.04)$ in the four redshift slices (for $k_{max} = 0.3\,h\,\mathrm{Mpc}^{-1}$). The magnitude of this error is less than half that of the statistical error in each bin. This systematic error represents the dispersion of growth-rate determinations within the set of redshift-space distortion models listed in Table 1.

We quote our final results using the Jennings et al. (2011) model, which usually produces the lowest value of χ^2, applied to $k_{max} = 0.3\,h\,\mathrm{Mpc}^{-1}$. The growth-rate measurements in the four redshift slices using this model, marginalizing over the other parameters, are $f = (0.60 \pm 0.10, 0.70 \pm 0.07, 0.73 \pm 0.07, 0.70 \pm 0.08)$. The values of the galaxy bias parameter in each redshift slice using this model, marginalizing over the other parameters, are $b^2 = (0.69 \pm 0.04, 0.83 \pm 0.04, 1.21 \pm 0.04, 1.48 \pm 0.08)$.

Fig. 7 explores in more detail the robustness of the growth-rate measurements as a function of k_{max} for the three optimal models. We plot the growth rate determined in four redshift slices for these models alone, considering a range of fitting limits between $k_{max} = 0.15$ and $0.3\,h\,\mathrm{Mpc}^{-1}$. Fig. 7 empirically demonstrates that systematic trends in the growth-rate measurement as k_{max} changes are typically less than the statistical error in the measurement for $k_{max} = 0.3$.

Fig. 8 displays the WiggleZ Survey measurements of the growth rate of structure in four redshift slices, using the Jennings et al. (2011) model with a variable damping parameter and fitting to $k_{max} = 0.3\,h\,\mathrm{Mpc}^{-1}$. We present our results multiplied by a redshift-dependent normalization, $f(z)\,\sigma_8(z)$, where $\sigma_8(z)$ is the rms fluctuation at redshift z of the linear matter density field in comoving $8\,h^{-1}$ Mpc spheres, calculated for our fiducial cosmological model. This weighting increases the model independence of the results by removing the sensitivity to the overall normalization of the power-spectrum model (Song & Percival 2009). Because the overall galaxy power-spectrum amplitude scales with $\sigma_8(z)\,b(z)$ at a particular redshift z, where $b(z)$ is the linear bias factor, and the magnitude of the redshift-space distortion due to coherent flows depends on $f(z)/b(z)$, then the measured value of the growth rate $f(z)$ scales as $1/\sigma_8(z)$. The weighted fits in the four redshift slices are $f(z)\,\sigma_8(z) = (0.42 \pm 0.07, 0.45 \pm 0.04, 0.43 \pm 0.04, 0.38 \pm 0.04)$. The WiggleZ measurements are compared to results previously published for the 2dFGRS, SDSS-LRG and VVDS samples, as collected by Song & Percival (2009), and to the prediction of a flat ΛCDM cosmological model with $\Omega_m = 0.27$. We note the following.
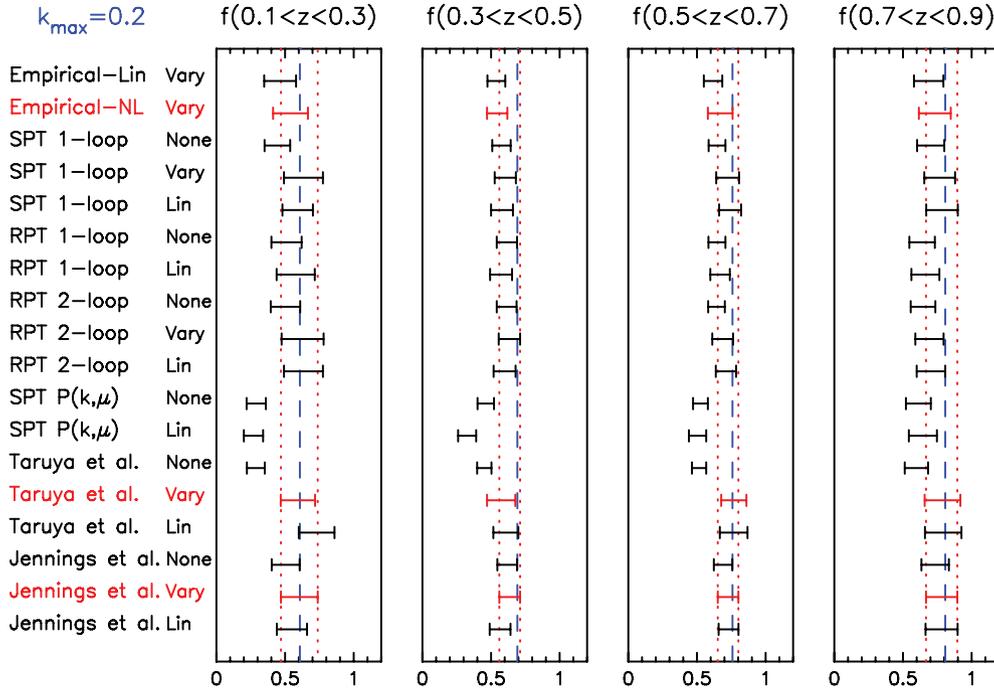
Figure 6. Measurements of the growth rate f in four redshift slices assuming a fitting limit $k_{max} = 0.2\,h\,\mathrm{Mpc}^{-1}$ for each of the 18 models listed in Table 1. The vertical dashed line indicates the prediction of a flat ΛCDM cosmological model with $\Omega_m = 0.27$. The two vertical dotted lines span the 68 per cent confidence region of the growth rate measured for the Jennings et al. model with a variable damping parameter, facilitating an easy comparison of the results for different models. The three best performing models (based on the values of the χ^2 statistic) are highlighted by the red text.
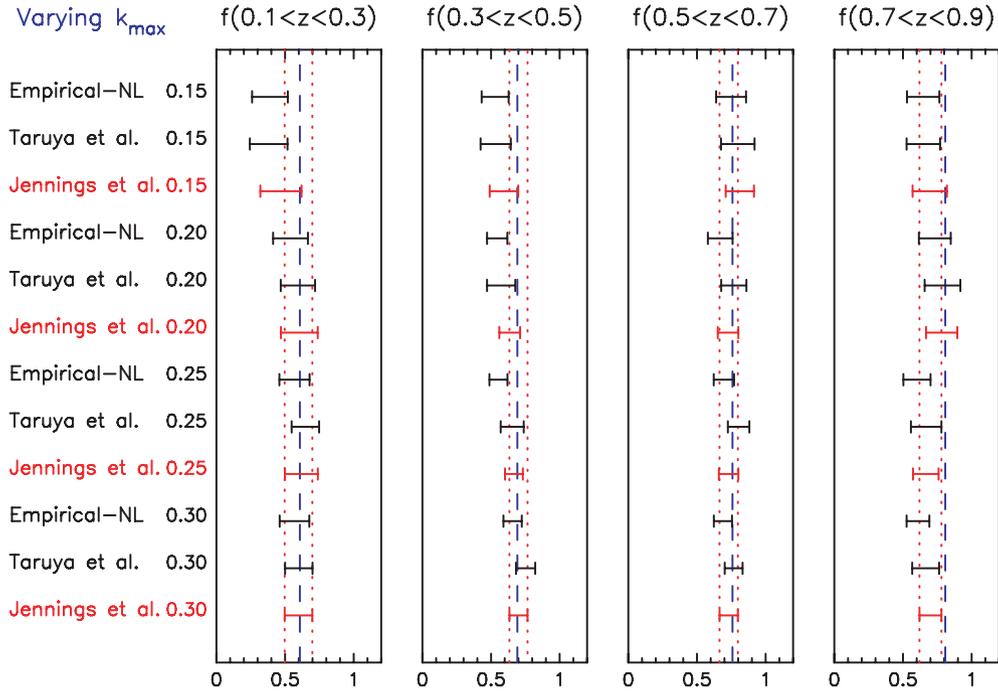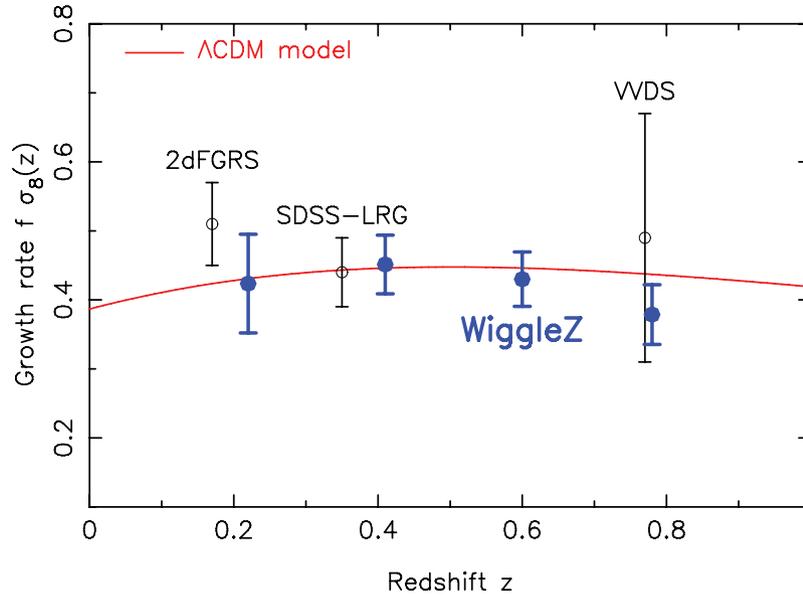

Figure 7. Measurements of the growth rate f in four redshift slices, varying the fitting limit k_{max} from 0.15 to $0.3\,h\,\mathrm{Mpc}^{-1}$ in steps of 0.05, for the three optimal models: the non-linear empirical Lorentzian, Taruya et al. (2010) and Jennings et al. (2011) models. All models include a variable damping parameter. The vertical dashed line indicates the prediction of a flat ΛCDM cosmological model with $\Omega_m = 0.27$. The two vertical dotted lines span the 68 per cent confidence region of the growth rate measured for the Jennings et al. model for $k_{max} = 0.3$, facilitating an easy comparison of the results for different models.

(i) The WiggleZ Survey data set is the first to produce precise growth-rate measurements in the intermediate-redshift range $z > 0.4$, the apparent transition epoch from decelerating to accelerating expansion, with 10 per cent measurement errors that are comparable to those obtained at lower redshift from existing surveys.

(ii) The low-redshift $z < 0.4$ WiggleZ measurements agree well with existing data.

Figure 8. Measurements of the growth rate of structure weighted by a redshift-dependent normalization, $f(z)\,\sigma_8(z)$, obtained in four redshift slices by fitting WiggleZ Survey data. We assume the Jennings et al. (2011) model for non-linear redshift-space distortions, with a variable damping parameter, and fit to the scale range $k < 0.3\,h\,\mathrm{Mpc}^{-1}$. The WiggleZ measurements are compared to results previously published for the 2dFGRS, SDSS-LRG and VVDS samples (black open circles) as collected by Song & Percival (2009). The prediction of a flat ΛCDM cosmological model with $\Omega_m = 0.27$ is also shown.

(iii) Our data set permits coherent flows to be quantified across the entire redshift range $z < 1$ using observations from a single galaxy survey.

(iv) A cosmological model in which general relativity describes the large-scale gravitation of the Universe, and the current matter density parameter is $\Omega_m = 0.27$, provides a good simultaneous description of the initial conditions described by CMB observations, the cosmic expansion history mapped by high-redshift supernovae and baryon acoustic oscillations, and the growth history mapped by galaxy bulk flows in the WiggleZ Dark Energy Survey.
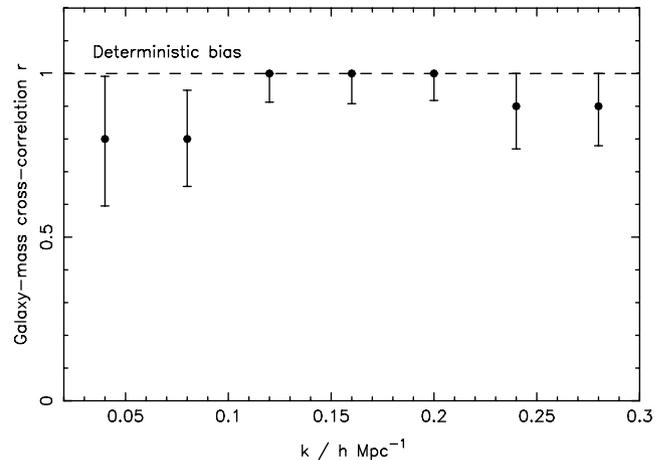
4.2 Galaxy–mass cross-correlation

In order to characterize the galaxy bias relation in more detail we introduced a cross-correlation parameter r between the galaxy and matter overdensities such that $\langle \delta_g \delta \rangle = br\langle \delta^2 \rangle$ and $\langle \delta_g^2 \rangle = b^2 \langle \delta^2 \rangle$ (where $|r| \leq 1$ is required by the definition of a cross-correlation coefficient). The value $r = 1$ corresponds to a fully deterministic bias, whereas $r \leq 1$ introduces a random stochastic element to the bias relation. Measurements of this stochasticity in the SDSS were presented by Swanson et al. (2008), who utilized a counts-in-cells analysis to quantify its dependence on scale, luminosity and colour. Swanson et al. found that a scale-independent deterministic linear bias was in general a good match to the SDSS data, especially on large scales, where the amplitude of the bias varied significantly with luminosity for red galaxies but not for blue galaxies. Furthermore, colour-dependent stochastic effects were evident at smaller scales. We can extend this analysis to higher redshifts using the WiggleZ power spectrum.

Equation (4) may be rewritten for a general cross-correlation parameter r as

$$P_g(k, \mu) = b^2 P_{\delta\delta}(k) - 2\mu^2 br\,P_{\delta\theta}(k) + \mu^4 P_{\theta\theta}(k), \qquad (14)$$

and assuming a model for the three power spectra $P_{\delta\delta}(k)$, $P_{\delta\theta}(k)$ and $P_{\theta\theta}(k)$, the value of r may be extracted for each scale k by marginal-

Figure 9. The galaxy–mass cross-correlation parameter r as a function of scale k, measured by fitting equation (14) to the WiggleZ power-spectrum data assuming the growth rate predicted by ΛCDM and marginalizing over a linear bias and variable damping factors. The measurements in different redshift slices are combined.

izing over b. In this investigation we fix the value of the growth rate f at the value predicted by the ΛCDM model, and we assume the Smith et al. (2003) and Jennings et al. (2011) prescriptions for the density and velocity power spectra. We also marginalized over a variable damping parameter.

Fig. 9 displays the measurement of r in independent Fourier bins of width $\Delta k = 0.04\,h\,\mathrm{Mpc}^{-1}$ between $k = 0.02$ and $0.3\,h\,\mathrm{Mpc}^{-1}$, combining the results for different redshift slices and varying r within the range $-1 \leq r \leq 1$. We find that the cross-correlation parameter is consistent with the deterministic bias $r = 1$ (and this result also applies for each separate redshift slice). Because the probability distribution for r is asymmetric due to the hard upper limit, in the cases when the confidence region is truncated at $r = 1$

we plot in Fig. 9 the range below $r = 1$ enclosing 68 per cent of the probability and the position of the peak of the likelihood.

5 ANALYSIS OF THE POWER-SPECTRUM MOMENTS

5.1 Multipole moments of the power spectrum

In this section we explore some alternative techniques for quantifying the redshift-space power spectra which can visualize their information content more neatly. The galaxy power spectrum $P_g^s(k, \mu)$ may be decomposed in a basis of Legendre polynomials $L_\ell(\mu)$ to give multipole moments $P_\ell(k)$:

$$P_g^s(k, \mu) = \sum_{\text{even } \ell} P_\ell(k) L_\ell(\mu), \tag{15}$$

$$P_\ell(k) = \frac{2\ell + 1}{2} \int_{-1}^{1} d\mu \, P_g^s(k, \mu) L_\ell(\mu). \tag{16}$$

The monopole ($l = 0$) spectrum primarily contains information about the underlying shape of the isotropic clustering pattern. The quadrupole ($l = 2$) spectrum holds the leading-order signal from the anisotropic modulation in power due to redshift-space effects. We note that the multipole moments may be expressed in terms of the density–velocity power spectra $P_{\delta\delta}$, $P_{\delta\theta}$ and $P_{\theta\theta}$ (e.g. Percival & White 2009).

The multipole moments may be extracted from the power-spectrum measurement in bins of μ by turning equation (16) from an integral into a sum:

$$P_\ell(k) = \frac{2\ell + 1}{2} \sum_{\mu \text{ bins}} P_g^s(k, \mu) \int_{\mu - \Delta\mu/2}^{\mu + \Delta\mu/2} L_\ell(\mu') \, d\mu' . \tag{17}$$

Alternatively, Yamamoto et al. (2006) introduced a direct estimator for $P_\ell(k)$ which does not require binning of the power spectrum in μ (which is particularly problematic at low k, where there are limited modes available in Fourier space). We present the key equations of the estimator here, referring the reader to Yamamoto et al. (2006) for the full derivation.

The Yamamoto et al. estimator, which is valid when the distant-observer approximation is applicable, is written using sums over N_{gal} observed galaxies and $N_{\text{ran}} = N_{\text{gal}}/\alpha$ random (mock) galaxies (where $\alpha \ll 1$). For each Fourier mode $\boldsymbol{k}$ we define the multipole moments based on the data as

$$D_\ell(\boldsymbol{k}) = \sum_{i=1}^{N_{\text{gal}}} w(\boldsymbol{s}_i) \exp(i\boldsymbol{s}_i.\boldsymbol{k}) L_\ell(\hat{\boldsymbol{s}}_i.\hat{\boldsymbol{k}}), \tag{18}$$

where $\boldsymbol{s}_i$ is the position vector of galaxy i and $w(\boldsymbol{s})$ is a weight factor for each galaxy, specified below. If we define the equivalent sum $R_\ell(\boldsymbol{k})$ over the set of random galaxies, then an estimator for $P_\ell(\boldsymbol{k})$ is

$$P_\ell(\boldsymbol{k}) = A^{-1} \left[D_\ell(\boldsymbol{k}) - \alpha R_\ell(\boldsymbol{k}) \right] \left[D_0(\boldsymbol{k}) - \alpha R_0(\boldsymbol{k}) \right] - S_\ell(\boldsymbol{k}), \tag{19}$$

where the shot noise term $S_\ell(\boldsymbol{k})$ is given by

$$S_\ell(\boldsymbol{k}) = A^{-1}(1 + \alpha)\alpha \sum_{i=1}^{N_{\text{ran}}} w(\boldsymbol{s}_i)^2 L_\ell(\hat{\boldsymbol{s}}_i.\hat{\boldsymbol{k}}). \tag{20}$$

The normalization A is given, in terms of sums over the N_c grid cells $\boldsymbol{x}$ constituting the window function, as

$$A = \sum_{\boldsymbol{x}} W^2(\boldsymbol{x}) w^2(\boldsymbol{x}) = \sum_{i=1}^{N_{\text{gal}}} W(\boldsymbol{s}_i) \, w^2(\boldsymbol{s}_i), \tag{21}$$

where $W(\boldsymbol{s})$ is the window function normalized over its volume V such that $\int W dV = N_{\text{gal}}$, or $\sum_{\boldsymbol{x}} W(\boldsymbol{x}) = N_{\text{gal}}(N_c/V)$. The minimum variance in $P_\ell(\boldsymbol{k})$ is produced by the usual FKP weight function

$$w(\boldsymbol{s}) = [1 + W(\boldsymbol{s})P_0]^{-1} , \tag{22}$$

where P_0 is a characteristic power-spectrum amplitude (which we take as $P_0 = 5000 \, h^{-3} \, \text{Mpc}^3$, although this choice has very little effect on our results). The error in the estimator for each Fourier mode $\boldsymbol{k}$ is given by

$$[\Delta P_\ell(\boldsymbol{k})]^2 = A^{-1}\alpha \sum_{i=1}^{N_{\text{ran}}} w(\boldsymbol{s}_i)^4 W(\boldsymbol{s}_i)$$
$$\times [W(\boldsymbol{s}_i)P(k) + 1 + \alpha]^2 [L_\ell(\hat{\boldsymbol{s}}_i \cdot \hat{\boldsymbol{k}})]^2. \tag{23}$$

We evaluated the estimator for $P_\ell(\boldsymbol{k})$ over the usual grid of Fourier modes which describe fluctuations in a cuboid of dimensions (L_x, L_y, L_z), i.e. for modes $\boldsymbol{k} = (k_x, k_y, k_z) = (2\pi n_x/L_x, 2\pi n_y/L_y, 2\pi n_z/L_z)$ for integers (n_x, n_y, n_z). We then averaged the amplitudes in spherical shells of $\boldsymbol{k}$ to produce our estimate of $P_\ell(k)$, which we write as $P_\ell^{\text{gridded}}(k)$. We note that the discreteness of the Fourier modes in the grid produces a bias in the estimate, which is particularly evident at low k. We corrected for this bias using a model power spectrum $P^{\text{model}}(\boldsymbol{k})$ by evaluating

$$P_\ell^{\text{model, gridded}}(\boldsymbol{k}) = A^{-1}\alpha \sum_{i=1}^{N_{\text{ran}}} w(\boldsymbol{s}_i)^2 W(\boldsymbol{s}_i)$$
$$\times P^{\text{model}}(\boldsymbol{k})L_\ell(\hat{\boldsymbol{s}}_i \cdot \hat{\boldsymbol{k}}), \tag{24}$$

which we averaged in spherical shells of k to produce $P_\ell^{\text{model, gridded}}(k)$, and also an exact determination using

$$P_\ell^{\text{model, exact}}(k) = \frac{2\ell + 1}{2} \int_{-1}^{1} d\mu \, P^{\text{model}}(k, \mu) L_\ell(\mu). \tag{25}$$

Our final estimate for the multipole power spectrum is then given by

$$P_\ell(k) = P_\ell^{\text{gridded}}(k) + P_\ell^{\text{model, exact}} - P_\ell^{\text{model, gridded}}. \tag{26}$$

We generated this correction using the best-fitting non-linear empirical Lorentzian redshift-space power spectrum (see Section 3.2) as the input model $P^{\text{model}}(\boldsymbol{k})$.

Fig. 10 compares the measurement of the multipole power spectra in four redshift slices obtained by the direct sum of equation (17) with the Yamamoto et al. estimator of equation (19). In general, the two different techniques for deriving the multipole power spectra agree well and we obtain measurements of the monopole ($\ell = 0$) and quadrupole ($\ell = 2$) with high signal-to-noise ratio. Current galaxy redshift surveys do not yield a significant detection of the hexadecapole ($\ell = 4$).

The final row of Fig. 10 plots the measured quadrupole-to-monopole ratio $P_2(k)/P_0(k)$ as a function of scale for each redshift slice. This statistic has the advantage of being less sensitive than the power spectrum itself to the parameters which model the shape of the underlying real-space galaxy clustering pattern (such as the background cosmological parameters or a scale-dependent bias). On large scales this ratio is expected to asymptote to a constant value which may be derived from equation (7):

$$\frac{P_2(k)}{P_0(k)} = \frac{(4/3)\beta + (4/7)\beta^2}{1 + (2/3)\beta + (1/5)\beta^2} , \tag{27}$$

where $\beta = f/b$. This value, indicated by the dotted 'linear' horizontal line in the bottom row of Fig. 10, and derived using the prediction
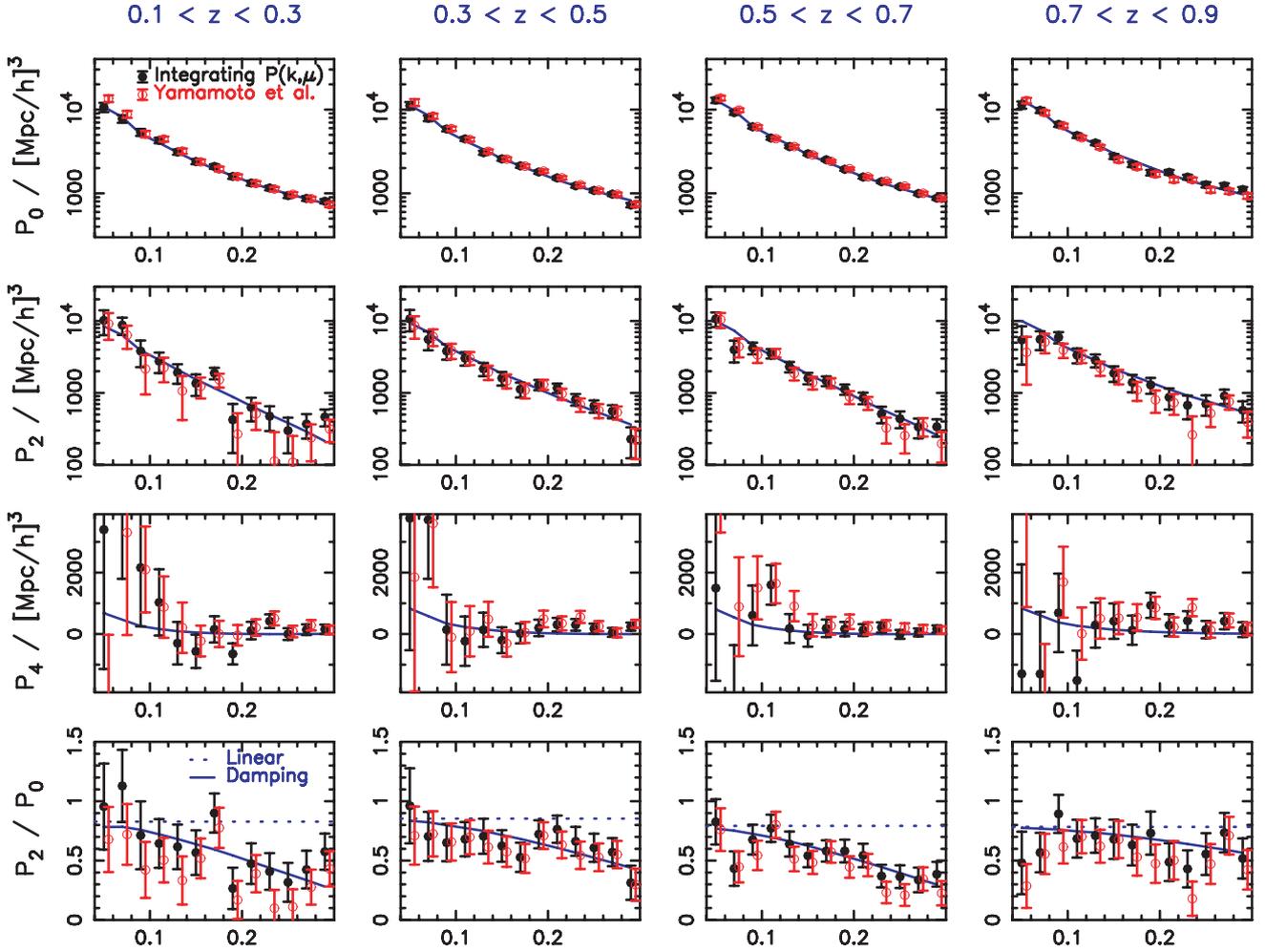
Figure 10. The multipole power spectra $P_\ell(k)$ for $\ell = 0, 2, 4$ for WiggleZ Survey observations in four redshift slices. The monopole ($l = 0$) spectrum primarily contains information about the underlying shape of the isotropic clustering pattern. The quadrupole ($l = 2$) spectrum holds the leading-order signal from the anisotropic modulation in power due to redshift-space effects. The (black) solid circles are generated from the stacked measurements of $P_g(k, \mu)$ across the different survey regions using equation (17). The (red) open circles, which are offset slightly in the x-direction for clarity, are generated by combining the estimates of $P_\ell(k)$ in each region using the Yamamoto et al. estimator of equation (19). The model lines correspond to the best-fitting non-linear empirical Lorentzian redshift-space distortion model in each case. The bottom row displays the quadrupole-to-monopole ratio $P_2(k)/P_0(k)$. Two models are overplotted: the large-scale Kaiser limit predicted in a ΛCDM cosmological model with $\Omega_m = 0.27$, labelled as 'linear', and the non-linear redshift-space distortion model, labelled as 'damping'.

of $f(z)$ in a ΛCDM model with $\Omega_m = 0.27$, lies in good agreement with the measurements on large scales in each redshift slice. At smaller scales the data deviate from this prediction due to the non-linear effects which damp the velocity power spectrum. We also plot the scale-dependent value of $P_2(k)/P_0(k)$ for the best-fitting non-linear empirical Lorentzian redshift-space distortion model in each redshift slice, indicated by the 'damping' line.

5.2 Power spectra of the velocity divergence field

The characteristic angular dependence of the redshift-space galaxy power spectrum $P_g^s(k, \mu)$ on its three component power spectra $P_{gg}(k)$, $P_{g\theta}(k)$ and $P_{\theta\theta}(k)$, exhibited by equation (4), gives us the opportunity to extract these three power spectra directly from data. This is of particular interest for the case of $P_{\theta\theta}(k)$ because this quantity depends on the growth rate but not on the galaxy bias, which is considered to be one of the principle sources of potential systematic error in redshift-space distortion model fitting.

The signal-to-noise ratio of the power-spectrum measurements from the current survey is not yet sufficiently high to extract three independent functions cleanly (e.g. Tegmark et al. 2004) – which is consistent with our failure to detect the hexadecapole in Fig. 10. However, a good approximation of the galaxy–velocity cross-power spectrum in the quasi-linear regime is $P_{g\theta} = -\sqrt{P_{gg}P_{\theta\theta}}$ (Percival & White 2009), which cancels (to first order) non-linear terms in the power spectra and galaxy bias. Under this approximation we can fit for the coefficients $P_{gg}(k)$ and $P_{\theta\theta}(k)$ in the model (Song & Kayo 2010) as

$$P_g^s(k, \mu) = P_{gg}(k) + 2\mu^2 \sqrt{P_{gg}(k)P_{\theta\theta}(k)} + \mu^4 P_{\theta\theta}(k). \quad (28)$$

For each separate k bin, spaced by $\Delta k = 0.02\,h\,\mathrm{Mpc}^{-1}$, we fitted the model of equation (28) to the stacked measurements of $P_g(k, \mu)$ from the WiggleZ Survey data set in four redshift slices. We performed the fit in 10 Fourier bins up to $k_{\max} = 0.2\,h\,\mathrm{Mpc}^{-1}$, choosing this upper limit because equation (4) will likely not provide a reliable description of the μ dependence of the power spectrum at smaller scales (given that our model fits in Section 4.1 favour the inclusion
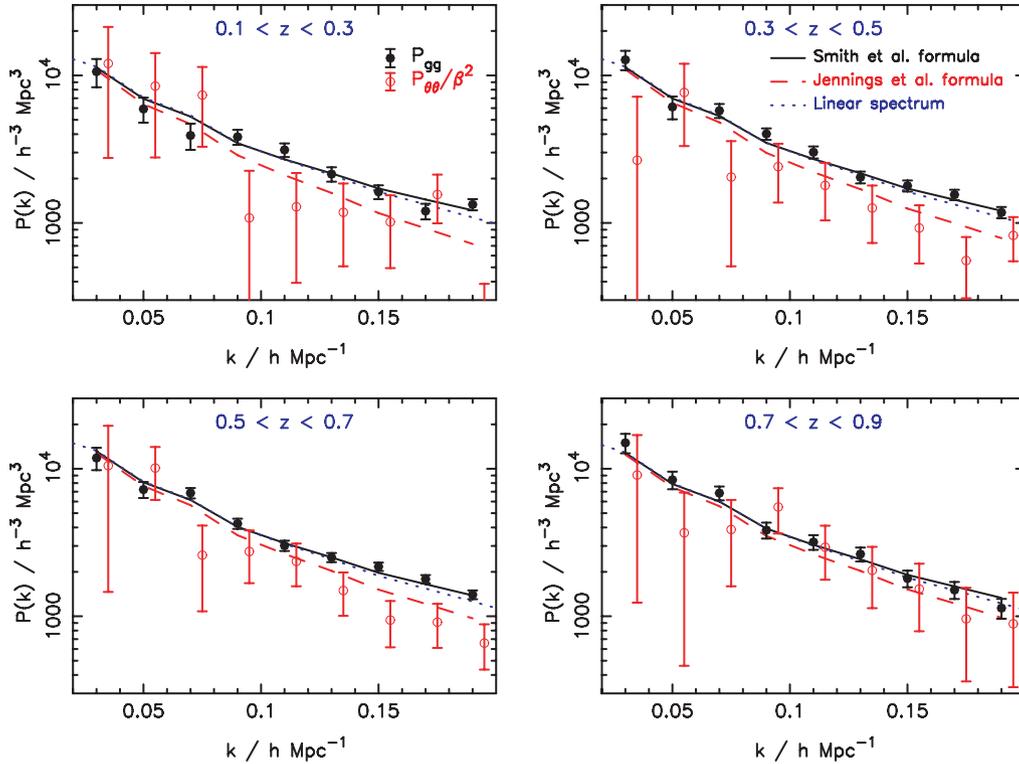
Figure 11. Measurement of the WiggleZ Survey galaxy–galaxy and velocity–velocity power spectra in four redshift slices by maximum-likelihood fitting to the stacked measurements of $P_g(k, \mu)$ across the different survey regions using the model of equation (28). The measurements of $P_{\theta\theta}$ are normalized by β^{-2} (in order to match the large-scale limit of P_{gg}) and are offset slightly in the *x*-direction for clarity. For comparison, we plot the linear-regime matter power spectra, the non-linear matter power spectra from Smith et al. (2003) and the non-linear velocity power spectra from Jennings et al. (2011). Our extraction of these two power spectra rests on the assumption that $P_{g\theta} = -\sqrt{P_{gg}P_{\theta\theta}}$ (Song & Kayo 2010), which has been validated at large scales by simulations (Percival & White 2009).

of an additional Lorentzian damping term over the range $0.2 < k < 0.3\,h\,{\rm Mpc}^{-1}$).

Fig. 11 displays the results of the fits for each redshift slice, where for convenience we have divided the measurements of $P_{\theta\theta}(k)$ by the best-fitting value of $\beta^2 = (f/b)^2$ so that the galaxy and velocity power spectra are expected to have the same large-scale limit. For comparison, we also plot in each case the non-linear galaxy and velocity power spectra based on the fitting formulae proposed by Smith et al. (2003) and Jennings et al. (2011), respectively, together with the underlying linear matter power spectrum for our fiducial cosmological parameters at these redshifts.

Our measurements constitute the first determination of the velocity power spectrum as a function of redshift and cleanly reveal the effects that we are modelling. At large scales $k < 0.1\,h\,{\rm Mpc}^{-1}$, the density and velocity power spectra are in close agreement with each other and with the input model linear power spectrum. At smaller scales the measurements diverge: the density power spectra are boosted in amplitude in a manner that closely matches the fitting formula of Smith et al. (2003), and the velocity power spectra are damped by non-linear effects. The fitting formula of Jennings et al. (2011) provides a good match to this damping: the value of χ^2 statistic is (13.4, 11.8, 12.4, 3.6) for the four redshift slices, respectively, for 10 degrees of freedom. The value of χ^2 for the highest redshift bin corresponds to a 2σ fluctuation. As the χ^2 values for the other three redshift slices fall within the 1σ range for the distribution, we do not view this with concern. We also find a tentative indication that the amplitude of the non-linear correction

to the velocity power spectrum increases with decreasing redshift, expected as a consequence of the growth of structure.

6 CONCLUSIONS

We have used the WiggleZ Dark Energy Survey data set to produce the first precise map of cosmic growth spanning the epoch of cosmic acceleration and the first systematic study of the growth history from a single galaxy survey. We have compared the measured power spectra to 18 different redshift-space distortion models using a combination of empirical models, fitting formulae calibrated by *N*-body simulations, and perturbation theory techniques. We itemize our conclusions as follows.

(i) Two quasi-linear redshift-space distortion models provide a good description of our data for scales $k < 0.3\,h\,{\rm Mpc}^{-1}$: the Taruya et al. (2010) model, incorporating extra angle-dependent correction terms in addition to the density and velocity power spectra from two-loop RPT, and the Jennings et al. (2011) fitting formula calibrated from *N*-body simulations. In each model we included a variable damping parameter. The growth rates deduced from these two very different modelling techniques agree remarkably well with the difference in values being much smaller than the statistical errors in the measurement. The level of this agreement gives us confidence that our results are not limited by systematic errors. We note that the empirical Lorentzian streaming model, where we use the non-linear matter power spectrum from Smith et al. (2003), also

performs well and the minimum chi-squared values for these three models typically differ by $\Delta\chi^2 \approx 1$. We quote our final results using the Jennings et al. (2011) model, which usually produces the lowest value of χ^2: growth-rate measurements of $f(z) = (0.60 \pm 0.10, 0.70 \pm 0.07, 0.73 \pm 0.07, 0.70 \pm 0.08)$ at redshifts $z = (0.22, 0.41, 0.6, 0.78)$, where we have marginalized over the variable damping factor and a linear galaxy bias factor. A more model-independent way of expressing these fits is $f(z)\sigma_8(z) = (0.42 \pm 0.07, 0.45 \pm 0.04, 0.43 \pm 0.04, 0.38 \pm 0.04)$.

(ii) These growth-rate measurements are consistent with those expected in a flat General Relativistic ΛCDM cosmological model with matter density $\Omega_m = 0.27$. Our observations therefore indicate that this model provides a self-consistent description of the growth of cosmic structure from perturbations and the large-scale, homogeneous cosmic expansion mapped by supernovae and baryon acoustic oscillations.

(iii) Assuming the growth rate predicted by the ΛCDM model we can fit for the parameters of a stochastic scale-dependent bias described by a galaxy–mass cross-correlation $r(k)$. We find that this bias is consistent with a deterministic model $r = 1$ for the range of scales $k < 0.3\,h\,\mathrm{Mpc}^{-1}$.

(iv) We considered various methods for presenting the information contained in the redshift-space power spectra, including deriving the multipole moments $P_\ell(k)$ using direct integration of the binned power spectrum $P(k, \mu)$ and by implementing the estimator described by Yamamoto et al. (2006). Measurements of the quadrupole-to-monopole ratio P_2/P_0 as a function of scale k delineate the influence of redshift-space distortions in a manner independent of the shape of the underlying matter power spectrum or a scale-dependent bias.

(v) Under the assumption $P_{g\theta} = -\sqrt{P_{gg}P_{\theta\theta}}$, which is a good approximation in the quasi-linear regime, we used the redshift-space power spectra to fit directly for $P_{gg}(k)$ and $P_{\theta\theta}(k)$. We found that (within an overall normalization factor) the galaxy and velocity power spectra are consistent with each other and with the model linear power spectrum at low k. For $k > 0.1\,h\,\mathrm{Mpc}^{-1}$ we delineated for the first time the characteristic non-linear damping of the velocity power spectrum as a function of redshift, with a tentative indication that the amplitude of the non-linear effects increases with decreasing redshifts. The Jennings et al. (2011) fitting formula provides a good fit to these power spectra.

A future investigation will involve the confrontation of these data with a range of modified-gravity models, combining the large-scale structure measurements with self-consistent fits to the CMB observations. Furthermore, a joint analysis of the redshift-space distortions and Alcock–Paczynski effect is also in preparation.

REFERENCES

Blake C. A. et al., 2009, MNRAS, 395, 240
Blake C. A. et al., 2010, MNRAS, 406, 803
Cabre A., Gaztanaga E., 2009, MNRAS, 393, 1183
Carlson J., White M., Padmanabhan N., 2009, Phys. Rev. D, 80, 3531
Cole S., Kaiser N., 1989, MNRAS, 237, 1127
Crocce M., Scoccimarro R., 2006, Phys. Rev. D, 73, 63519
da Angela J. et al., 2008, MNRAS, 383, 565
Davis T. M. et al., 2007, ApJ, 666, 716
Dekel A., Lahav O., 1999, ApJ, 520, 24
Drinkwater M. et al., 2010, MNRAS, 401, 1429
Eisenstein D. J., Hu W., 1998, ApJ, 496, 605
Feldman H. A., Kaiser N., Peacock J. A., 1994, ApJ, 426, 23 (FKP)
Gilbank D. G., Gladders M. G., Yee H. K. C., Hsieh B. C., 2011, AJ, 141, 94
Guy J. et al., 2010, A&A, 523, 7
Guzzo L. et al., 2008, Nat, 451, 541
Hamilton A. J. S., 1998, in Hamilton D., ed., The Evolving Universe. Kluwer, Dordrecht, p. 185
Hatton S., Cole S., 1998, MNRAS, 296, 10
Hawkins E. et al., 2003, MNRAS, 346, 78
Jennings E., Baugh C. M., Pascoli S., 2011, MNRAS, 410, 2081
Jing Y., 2005, ApJ, 620, 559
Juszkiewicz R., Sonoda D. H., Barrow J. D., 1984, MNRAS, 209, 139
Kaiser N., 1987, MNRAS, 227, 1
Komatsu E. et al., 2009, ApJS, 180, 330
Lau E. T., Nagai D., Kravtsov A. V., 2010, ApJ, 708, 1419
Lewis A., Challinor A., Lasenby A., 2000, ApJ, 538, 473
Linder E., 2005, Phys. Rev. D, 72, 3529
Linder E., Cahn R., 2007, Astropart. Phys., 28, 481
Linder E., Jenkins A., 2003, MNRAS, 346, 573
Matsubara T., 2008, Phys. Rev. D, 77, 063530
Nesseris S., Perivolaropoulos L., 2008, Phys. Rev. D, 77, 023504
Nishimichi T. et al., 2009, PASJ, 61, 321
Okumura T., Jing Y. P., 2011, ApJ, 726, 5
Okumura T., Matsubara T., Eisenstein D. J., Kayo I., Hikage C., Szalay A. S., Schneider D. P., 2008, ApJ, 676, 889
Peacock J. A. et al., 2001, Nat, 410, 169
Percival W. J., White M., 2009, MNRAS, 393, 297
Percival W. J. et al., 2004, MNRAS, 353, 1201
Percival W. J. et al., 2010, MNRAS, 401, 2148
Raccanelli A., Samushia L., Percival W. J., 2010, MNRAS, 409, 1525
Reid B. A. et al., 2010, MNRAS, 404, 60
Rimes C. D., Hamilton A. J. S., 2005, MNRAS, 360, 82
Rubin D. et al., 2009, ApJ, 695, 391
Scherrer R. J., Weinberg D. H., 1998, ApJ, 504, 607
Scoccimarro R., 2004, Phys. Rev. D, 70, 083007
Sharp R. et al., 2006, in McLean I. S., Iye M., eds, Proc. SPIE Vol. 6269, Ground-based and Airborne Instrumentation for Astronomy. SPIE, Bellinghan, p. 62690G
Smith R. E. et al., 2003, MNRAS, 341, 1311
Song Y.-S., Kayo I., 2010, MNRAS, 407, 1123
Song Y.-S., Percival W. J., 2009, J. Cosmol. Astropart. Phys., 10, 4
Swanson M. E. C., Tegmark M., Blanton M., Zehavi I., 2008, MNRAS, 385, 1635
Takahashi R. et al., 2011, ApJ, 726, 7

Taruya A., Nishimichi T., Saito S., 2010, Phys. Rev. D, 82, 3522
Tegmark M. et al., 2004, ApJ, 606, 702
Tegmark M. et al., 2006, Phys. Rev. D, 74, 123507
Vishniac E. T., 1983, MNRAS, 203, 345
Wang Y., 2008, J. Cosmol. Astropart. Phys., 5, 21
Wiltshire D. L., 2009, Phys. Rev. D, 80 123512

Yamamoto K., Nakamichi M., Kamino A., Bassett B. A., Nishioka H., 2006, PASJ, 58, 93

This paper has been typeset from a T$_{\rm E}$X/L$^{\rm A}$T$_{\rm E}$X file prepared by the author.